

# Real-time imaging of slow noisy quasiparticle dynamics at a non-trivial metastable defect in an electronic crystal.

Y. Vaskivskyi<sup>1,3</sup>, J. Vodeb<sup>1,2,4</sup>, I. Vaskivskyi<sup>1,3,4</sup>, and D. Mihailovic<sup>1,3,4</sup>

<sup>1</sup>*Jozef Stefan Institute, Jamova 39, 1000 Ljubljana, Slovenia*

<sup>2</sup>*Jülich Supercomputing Centre, Institute for Advanced Simulation, Forschungszentrum Jülich, 52425 Jülich, Germany,*

<sup>3</sup>*Faculty of Mathematics and Physics, University of Ljubljana, Ljubljana, Slovenia*

<sup>4</sup>*CENN Nanocenter, Jamova 39, 1000 Ljubljana, Slovenia*

**Nonequilibrium self-assembly is the root of all emergent complexity, including life. In quantum materials emergent metastable states have become a very fashionable topic of research, but the study of resulting mesoscopic state dynamics is hindered by the absence of appropriate methods. Here we pioneer the use of fast-scanning tunnelling microscope (FSTM) techniques to investigate the internal dynamics of mesoscopic metastable topologically non-trivial defects in an electronic Wigner crystal superlattice created by a local electromagnetic perturbation. This allows us to record unprecedented individual electron motion trajectories in real-time on the millisecond timescale. Such dynamics is understood to arise from coupling of hybridised Goldstone-Higgs bound states localised at the Y junction with microscopic electronic degrees of freedom that lead to the formation of localised quasiparticles with slow internal dynamics. Their unprecedented robustness against external perturbations comes from non-local constraints and non-trivial broken symmetries. Two-level system ‘telegraph’ noise maps at the junction show phase and amplitude that is correlated with the observed electron motion trajectories. Such observation of single-particle dynamics in real time fundamentally transforms our understanding of metastable quantum states in electronic crystals and paves the way for technological advancements that make use of engineered topologically non-trivial defects.**

The choreography of self-assembly in nonequilibrium systems is governed not only by symmetry, topology and causality constraints<sup>1,2</sup>, but also by a temporally evolving spatially non-uniform ambient environment. Such situations arise anywhere from rapid crystal growth on surfaces to molecular self-assembly in biological systems and in quantum many-body systems. In principle, by guiding the trajectory of the nonequilibrium system with appropriate initial and boundary conditions we may engineer the formation of topologically and symmetry-protected mesoscopic metastable states with new and interesting emergent properties. Of interest are states that show robustness against external perturbations, particularly if they harbour dynamics on an energy scale which is below the thermal energy scale<sup>3,4</sup>. Electronic crystals are an excellent playground for experimentally investigating such behaviour as they controllably form metastable domains and topological defects associated with domain wall junctions in the electronic superlattice after rapid self-assembly<sup>5–10</sup>. Robust topological defects - solitons have previously been imaged by scanning-tunneling microscopy (STM) in quasi-1D systems<sup>11</sup>. In 2D, the topological structure of such states is more complex, but it was shown that it can be controlled and manipulated by external perturbation<sup>12</sup>, while domain walls have been shown to contain low-energy states and as yet unidentified sources of noise<sup>13,14</sup>.

Here - using a localised transient electrical perturbation with an STM tip, we first create a topologically non-trivial Y-junction defect at the intersection of three domains. Using a fast-scanning tunnelling microscope (FSTM) we then record movies of density of states fluctuations in *real time* that correspond to motion of *individual electrons* localised within the defect. 2D maps of tunnelling current temporal fluctuations reveal localised emergent two-level system (TLS) ‘telegraph’ noise whose analysis leads to very detailed picture of the mesoscopic emergent quasiparticle states and poses fundamental questions on the origin of its slow dynamics and unprecedented robustness to external perturbations.

The electronic crystal chosen for this investigation is 1T-TaS<sub>2</sub>, a layered transition metal dichalcogenide (Fig. 1a) which exhibits a propensity for electron localization. In quasi-equilibrium polarons order into

different charge-density wave (CDW) states at different temperatures<sup>15–19</sup>. The polaron structure is in the form of a distorted hexagram as shown in Fig. 1a (ii)<sup>17</sup>. The low-temperature ground state is a commensurate (C) insulating  $\sqrt{13} \times \sqrt{13}$  superlattice<sup>16,17</sup> (Fig. 1a (iii)), with two possible orientations,  $\chi_L$  and  $\chi_R$  relative to the crystal axes, related to each other by mirror symmetry  $\sigma$ <sup>20,21</sup>.

To create a topologically non-trivial embedded defect on the surface, we apply an electrical pulse through a sharp STM tip which locally destroys the C order<sup>12,22,23</sup>. Rapid spontaneous self-assembly of polarons results in a mesoscopic network of topologically non-trivial domain walls and vertices<sup>8,10,12</sup> that can be manipulated by tip or externally sourced current<sup>12</sup> (Fig. 1a iv). Fig. 1b shows a time-averaged topographic FSTM image of a Y-junction vertex forming at the intersection of three domains (labelled A, B and C) within such a structure. A schematic construction of the Y-junction is shown in Fig. 1c, showing the polaron positions (denoted as idealized hexagrams) at the domain boundary. Domains A and B both have the same chirality ( $\chi_L$ ), while domain C has  $\chi_R$  chirality. Choosing a clockwise path, A and B are related to each other via a translation vector  $\mathbf{T}_{A \rightarrow B} = (3\mathbf{a} - \mathbf{b})$ , where  $\mathbf{a}$  and  $\mathbf{b}$  are crystal lattice constants (Fig. 1c). B and C are related by a mirror operation  $\sigma_{\mathbf{a}-\mathbf{b}}$  about the  $\mathbf{a} - \mathbf{b}$  axis followed by a translation  $-\mathbf{b}$ , while A and C are related by a combination of a mirror operation  $\sigma_{\mathbf{a}}$  about the  $\mathbf{a}$  axis, followed by a translation  $-\mathbf{a}$ . A schematic image of the CDW order at the vertex corresponding to the FSTM image 1b is shown in Fig. 1d.

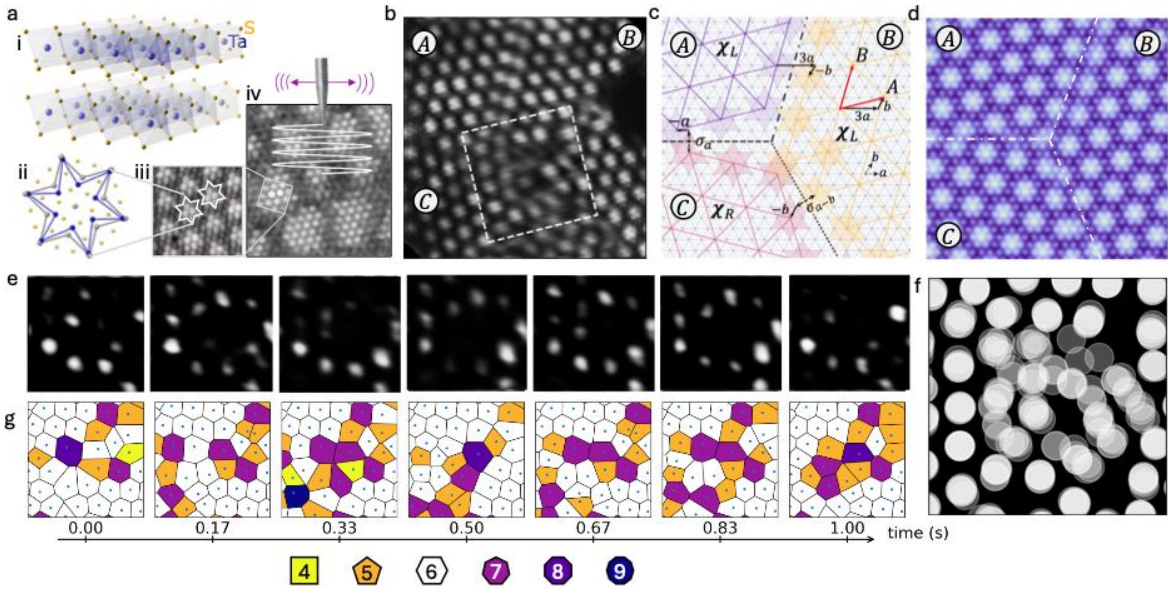


**Figure 1 Real-time dynamics of semi-localized electrons in vertex trap.** a) (i) The crystal structure of 1T-TaS<sub>2</sub>, (ii) the polaronic lattice distortion at different temperatures<sup>17</sup> and (iii) high-resolution STM topography of the C CDW state. (iv) the domain state created by external perturbation with a schematic description of the fast-scanning STM measurement. b) The 7 minute time-average of an STM movie (SV1 and SV2) recorded with the STM tip at a constant height above the surface ( $V = 0.4$  V,  $i = 1.5$  nA) shows continuity of QP motion. c) The vertex structure showing broken mirror and translational symmetries, indicated by the vector constructions at the domain walls. d) The order parameter  $\Psi_{\text{CDW}}(\mathbf{x})$  at the vertex corresponding to b) and c) (the Ta atoms in the crystal lattice are also visible). e) A set of extracted frames measured 0.17 seconds apart extracted from the full frame showing quasi-periodic individual polaron motion (see SV3 for full movie). f) A time-averaged image emphasizing polaron motion. The trajectories are analysed in Fig. 3. g) a W-S tessellation of e) showing 5-gon-7-gon and 4-gon-8-gon dislocations as well as single  $n$ -gon disclinations. A full movie is available in the supplement (SV4).

The temporal and spatial current fluctuations  $i(\mathbf{r}, t)$  in the vertex recorded by a FSTM reveal real-time motion of individual polarons. A movie recorded with constant tip height (voltage) over an area of  $15 \times 15 \text{ nm}^2$  at a frame rate of  $R_F \sim 6 \text{ fps}$  (25 MHz sampling rate,  $T = 77$  K) is shown in SV1. Fig. 1e shows a short sequence of frames extracted from the movie (SV2) showing polaron movements in time on the millisecond timescale ( $\tau \sim 10 \text{ ms}$ ). The time-integrated polaron positions (depicted by circles) are shown in Fig. 1f, emphasizing the polaron trajectories. The observed strongly sub-thermal fluctuations ( $kT \gg \hbar v$ ) are persistent on the timescale of the experiment (7 minutes). Dislocations (DL) and disclinations (DC) associated with moving polarons are revealed by a Wigner-Seitz (W-S)

tessellation (Fig. 1g) and appear as pentagon/heptagon pairs or individual  $N - gons$  ( $N = 4, 5, 7, 8$ ). Such defects are important, as they are topologically protected which can lead to arrested charge dynamics<sup>24,25</sup>. The full movie (SV4) of defect dynamics shows that DCs occur primarily at the intersection of the  $\chi_L/\chi_R$  domains and along B-C domain walls (DWs). DLs are present at the  $T$ -symmetry-breaking DW boundary and show quite lively dynamics on the millisecond timescale (see SV4).

Time-series plots of the temporal and spatial fluctuations of the tip current  $i(\mathbf{r}, t)$  for a few chosen positions  $\mathbf{r}$  identified by coloured dots in Fig. 2d are shown in Fig. 2a. (A larger data set is presented in the SI). We clearly identify two types of behaviour: (i) TLS telegraph noise in regions where particle motion is observed, and (ii) ‘single-level’ noise far from these regions. The corresponding current distribution  $\theta(i(\mathbf{r}, t))$  is shown in Fig. 2b. Further, we observe in Fig. 2a that the telegraph noise of trace 3 has *opposite phase* compared with traces 1, 2 and 4. Thus, we note that the overall TLS behaviour is coherent: the effective phase relation between the pixels  $\phi(t)$  is maintained throughout the duration of the measurement even for pixels that are far apart (see SI). A map of  $\phi(\mathbf{r})$  in Fig. 2f shows phase modulations across the entire image, with reference to the phase of the centre of the vertex.

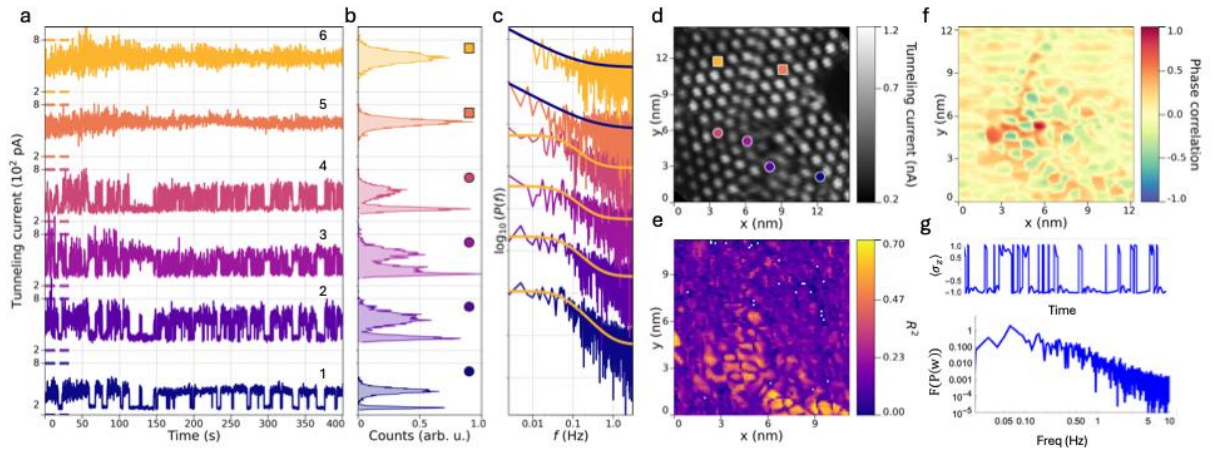


**Figure 2 Noise analysis of charge fluctuations.** a) Time-traces of tunnelling current  $i(\mathbf{r}, t)$  recorded at constant tip height at a few selected points shown in d). They show temporally correlated ‘telegraph noise’ traces (1-4) with  $0$  or  $\pi$  phase shift  $\phi$ , or featureless noise (traces 5 and 6). b) The dwell time distributions for the traces shown in a) showing either single level or TLS behaviour. c) Fits to the power spectra of  $i(\mathbf{r}, t)$  at points shown in a) give either flat-top Lorentz spectra with  $1/f^2$  tails or  $1/f$  noise with frequency-independent tails at high  $f$ . e) A pixel map of the amplitude of TLS noise expressed as the fit confidence factor  $r^2$  of Lorentz fits to  $F(i(\mathbf{r}, t))$  shown in d). f) A map of the variation of phase  $\phi(\mathbf{r})$  across the vertex space. g) Level occupancy  $\langle \sigma^2 \rangle$  and power spectrum  $F(P(w))$  for an external noise-driven model TLS system.

Fourier power spectra  $F_t(i(\mathbf{r}, t))$  corresponding to the temporal current fluctuations  $i(\mathbf{r}, t)$  are shown in Fig 2 c. In the regions that show telegraph noise  $F_t(i(\mathbf{r}, t))$  clearly show characteristic ‘flat-top’ Lorentzian curves  $L(f)$  (Fig. 2c) with a  $1/f^2$  high-frequency tail. Elsewhere we ubiquitously see  $1/f$  power spectra - attributed to current originating from many TLSs with different level spacings<sup>13,26–28</sup>. These areas show no saturation at low frequencies and exhibit frequency-independent ‘white’ noise at high frequencies, presumed to be of thermal origin. Separating the three different noise contributions  $S = L(f) + \beta/f + \gamma$  for each pixel, we can spatially separate TLS noise from  $1/f$  noise, and obtain high resolution maps of the amplitude (Fig 2f) of the TLS noise source.

In addition to the amplitude and phase fluctuations of  $i(\mathbf{r}, t)$  above, plotting the polaron *centre positions* in the  $x - y$  plane as a function of time (Fig. 3 a), we see that some particles appear to show dumbbell-like oscillating motion (Fig. 3b). The polaron motion patterns are also clearly discernible in the FSTM movies (SV1 and SV2). To examine if and how these displacements are correlated, in Fig. 3 c and d we present an analysis of the positional correlations of pairs of polarons. The coloured dots depict the correlations between pairs of adjacent polarons along the  $x$  and  $y$  coordinates (see SI for details). We observe particularly non-trivial polaron motion at the vertex core. For example, an abrupt change from symmetric (red dots) to antisymmetric polaron-pair displacements (blue dots) is visible at the centre of the vertex. Further away from the vertex, the displacements along the  $T$ -symmetry-breaking A-B DW boundary show antisymmetric motion, seen as a line of pale blue dots along the A-B domain wall.



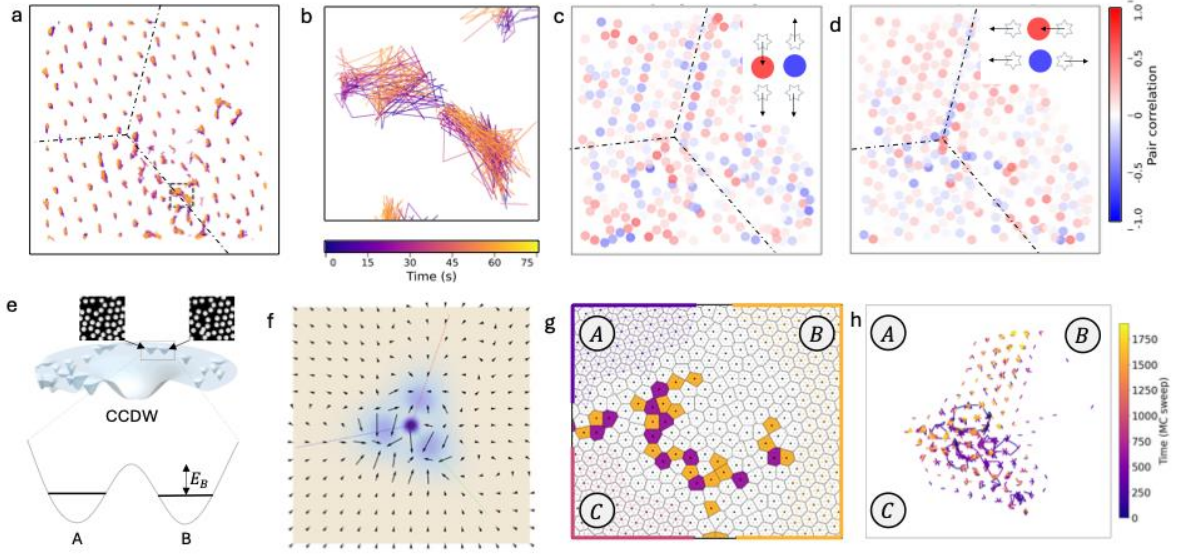


**Figure 3 Inter-particle motion correlations and modelling of Y-junction dynamics.** a) and b) the measured spatial trajectory of polarons. The timeline is indicated by the colour bar. c) The polaron-pair displacement correlation coefficient  $\xi$  (indicated by colour) along the x direction and d) the y direction. The displacements are defined by the legend. Note the cross-over from symmetric to antisymmetric motion at the vertex core. e) An energy landscape describing the domain configurational space. Neighbouring configurational states described by a double well potential giving rise to TLS behaviour shown in Fig. 2g. f) A model simulation showing  $\Delta^2(\mathbf{r}, t)$  (blue colour) and vector field proportional to the gradient  $\nabla\phi(\mathbf{r}, t)$  for the low-energy branch of the hybridised Higgs-Goldstone mode. (See movie [SV5](#) for the temporal fluctuations. g) A MC simulation of defect time evolution. See [SM7](#) for full movie. h) local MC polaron trajectories (See also [SV8](#)).

As an aid to understanding the dynamics we first consider transitions between minima on a configurational energy landscape (Fig. 3e). The ground state (bottom of the funnel) corresponds to the uniform global C superlattice, while the auxiliary minima around the rim of the ‘Mexican hat’ correspond to different domain configurations. The telegraph noise, flat-top power spectra and state occupation distributions in Fig. 2 can be reproduced by using either a noisy open quantum TLS system simulation of Lindblad dynamics (for low T) or a classical Langevin equation for a non-linear driven oscillator (Fig. 2g, see SI for calculations). On the other hand, estimating the frequency of thermally activated dynamics across a barrier using the classical formula  $\nu = \nu_0 e^{-E_B/k_B T}$  with  $E_B = 10 \sim 20$  meV obtained experimentally<sup>29,30</sup> and using the collective amplitude mode frequency  $\nu_0 = 2.5$  THz<sup>31</sup> for 1T-TaS<sub>2</sub>, at 77 K we find that  $\nu = 0.1 \sim 0.6$  THz which is much too fast to describe the observed dynamics. So thermally activated transitions between minima in the configurational landscape do not really give a useful quantitative timescale estimate for the observed dynamics.

Turning to the collective excitations, the homogeneous CDW order parameter for the C state is written as  $\Psi(\mathbf{r}, t) = \Delta(\mathbf{r}, t)e^{i\phi(\mathbf{r}, t)}$ , where  $\Delta(\mathbf{r}, t)$  is the ‘Higgs’ amplitude,  $\mathbf{Q}_i$  are the reciprocal lattice vectors that define the CDW superlattice,  $\phi$  controls the phason or ‘Goldstone mode’. In C systems the Goldstone mode is gapped with an energy scale corresponding to the pinning energy<sup>26</sup>. Approaching the Y junction, the order parameter is suppressed as  $\Delta(\mathbf{r}, t) \rightarrow 0$  and the local fluctuations of the phase stiffness  $K(\mathbf{r}, t) \propto \Delta(\mathbf{r}, t)^2$  slow down and diverge in relative magnitude as  $\frac{\delta K(\mathbf{r}, t)}{K} \sim \frac{\delta \Delta(\mathbf{r}, t)}{\Delta}$  when  $\Delta(\mathbf{r}) \rightarrow 0$ . Furthermore, due to broken symmetries at the vertex core and in the arms of the Y-junction (the DWs), mixing between the ‘Higgs’ mode and the Goldstone mode leads to a low-frequency hybrid branch localised at the vertex core. The fluctuations of the phase are primarily longitudinal along the DWs, but also include a skew, arising from the non-trivial broken symmetries at the DWs comprising the Y junction. The phase currents  $\mathbf{j}_\phi(\mathbf{r}, t) = -K(\mathbf{r}, t)\nabla\phi(\mathbf{r}, t)$  depicted by the arrows in Fig. 3f are driven by the STM tip scanning motion to periodically breathe and shear. The movie [SV5](#) shows the

temporal fluctuations of  $\mathbf{j}_\phi(\mathbf{r}, t)$  along the DWs and at the junction. Although the model calculation is a significant simplification, and does not take into account extrinsic imperfections seen in Fig. 1d, or interaction with the background band electrons or other crystal layers, the experimentally observed motion (SV2) bears a resemblance to the order parameter fluctuations of the low-frequency hybridised mode. The resulting noise spectrum  $S_k(\mathbf{r}, \omega) = \int dt e^{i\omega t} \langle \delta K(\mathbf{r}, t) \delta K(\mathbf{r}, 0) \rangle$  is strongly enhanced and shifted to low frequencies, with the appearance of telegraph-like noise accompanying local polaron reconfigurations and recovering the Langevin dynamics. A higher frequency hybrid mode also occurs when the phase field forms a continuous circulation around the core of the Y junction. (A detailed calculation and movies of the order parameter fluctuations are shown in SV5 and SV6). At low temperatures the Y-junction provides a platform for the formation of a topologically protected qubit reminiscent of delocalised molecular-like orbitals, where the level splitting is controlled by the CDW phase flux described above. When two domain walls break  $\sigma$  and  $T$  symmetry and one breaks  $T$  symmetry, the overall symmetry is reduced to C1, leading to unequal electron hoppings and on-site energies which results in a circulation. The charge density  $\rho_i = |\langle i | \psi(t) \rangle|^2$  and local currents  $J_{ij} \propto \text{Im} [t_{ij} e^{i\phi_{ij}} \psi_i^* \psi_j]$  describe the vertex dynamics, whereby the  $|0\rangle$  state exhibits stationary, symmetric density, while the  $|1\rangle$  state carries circulating currents corresponding to phase winding around the vertex. The emergent quasiparticle at the Y-junction thus combines the hybridised collective modes with a topologically protected bound electronic state to form a composite quasiparticle localised at the vertex exhibiting complex emergent dynamics.

Finally, let us examine microscopically the correlated polaron ordering dynamics and local defect formation within the Y-junction shown in Fig. 1g. Using the model Hamiltonian<sup>19</sup>  $H = - \sum_{i,j} t_{ij} c_i^\dagger c_j + \sum_{i<j} V_{i,j} n_i n_j$  where  $t_{i,j}$  is the polaron tunnelling amplitude between sites  $i$  and  $j$ ,  $V_{i,j} = \frac{V_0}{r_{ij}} \exp\left(-\frac{r_{ij}}{r_s}\right)$  is the Coulomb screening potential,  $r_s = 4.5 a \sim 1.5 \text{ nm}$  is the screening radius,  $V_0 = \frac{e^2}{\epsilon_0 a} \sim 1 \text{ eV}$ , and  $a$  is the lattice constant, we assume that polaron hopping is negligible compared with the mutual Coulomb repulsion and that external noise is the driver of polaron dynamics, which is consistent with previous low-T measurements of domain fluctuations<sup>30</sup>. Imposing non-local symmetry constraints of the Y-junction by fixing the boundary conditions at the edges, the polaron defect dynamics can be calculated using a classical Monte Carlo (MC) simulation. Figs. 3g and h reveal the time evolution of DC and DL defects (shown as a W-S tessellation) which qualitatively match the observed defect dynamics in Fig. 1g, effectively demonstrating the effect of non-local constraints on the formation of the defects at the Y junction. A full movie of the dynamics in SV7 showing the collapse of the defects into dislocation chains along the two DWs in the Y junction that break mirror symmetry. The MC polaron trajectories are shown in Fig. 3h (and SV8) showing close resemblance to Fig. 3a. We note that such charged defect motion with drastically arrested mobility may be described in terms of fractons – recently postulated quasiparticles whose motion is governed by higher moment conservation laws – particularly DL dipoles<sup>24,32</sup> which – driven by the hybridised collective modes is consistent with the slow single particle motion observed experimentally.

We conclude that FSTM mapping measurements of emergent metastable state fluctuations pioneered by this work could be used to identify, characterise and control such TLSs on different levels in other systems such as glasses<sup>33,34</sup>, or more generally - quantum materials where defects appear in the process of fabrication<sup>28,35</sup> or are introduced on purpose<sup>12</sup> for building circuits.

## Methods

The Elettra Sincrotrone fast scanning STM module is implemented on a Scienta-Omicron Nanoprobe LT system and records the tunnelling current  $i_t(V)$  from the Pt tip to surface of the 1T-TaS<sub>2</sub> crystal with a tip that controllably oscillates laterally across the sample surface (Fig. 1a). The measured STM tunnelling current at time  $t$  and position  $\mathbf{r}$  is  $i(\mathbf{r}, t) \propto |M_{\text{tip-sample}}|^2 D_s(\mathbf{r}, t)$ , where  $M_{\text{tip-sample}}$  is the usual matrix element for the tunnelling transition between the tip states and the sample,  $D_s(\mathbf{r}, t)$  is the density of states at the surface of the sample at any given time  $t$ . The total current  $i(\mathbf{r}, t)$  is an incoherent integration over time of the individual electron tunnelling currents as the tip moves across

the sample. The  $V - i$  curves in conventional scanning mode are consistent with those reported previously<sup>8,10,22,23</sup>. The  $V$  and  $i$  parameters are shown in the figure captions for each case. In the C state, the bright ‘blobs’ approximately correspond to individual polarons. In the vertex region and in the domain walls the CDW acquires non-trivial time-dependent phase fluctuations  $\delta(\mathbf{r}, t)$ , so this approximation is no longer valid, and  $D_s(\mathbf{r}, t)$  is determined by the structure of microscopic electronic wavefunctions<sup>8,10,22,23</sup>. The FAST STM typically records  $100 \times 100$  pixel image sequences with a tunnelling current sampling rate of 25~100 MHz, averaged typically for 10~20  $\mu$ s per pixel limited by the amplifier bandwidth (400 kHz), recorded line-wise (Fig. 1b) resulting in frame rates  $R_F = 5\sim 100$  Hz. Note that all dynamics that is slower than individual frame recording time  $t > \tau_{frame} (\sim 0.1 \text{ s})$  is visible as real-time motion. Dynamics that occurs on timescales  $\tau_{frame} > t > \tau_{pixel} (\sim 10^{-8} \text{ s})$  leads to temporal and spatial distortions of the images. Faster dynamics with  $t \ll \tau_{pixel}$  averages out and the structure appears static. If there is no motion blur, the FTSM gives atomic-resolution images (See SI). A large language model was used as a Mathematica programming aid for parts of the simulations shown in Fig. 3f and 2g and the Supplement. The codes are available in the depository.

## Author contributions

The experimental work was performed by Y.V. and I.V.. The data analysis was performed Y.V., D.M. and J.V.. All authors contributed to the conceptual discussions. Theoretical modelling was performed by J.V. and D.M.. The paper was written by D.M. with contributions from all authors.

## Acknowledgments

We wish to acknowledge discussions with Viktor Kabanov, Lev Vidmar, Leo Radzihovski, Alexei Kitaev, Duncan Haldane, Mikhail Feigelman, Anton Zeilinger, Michel Devoret, Rok Zitko, Denis Golež and Serguei Brazovskii. The project was funded by ARIS funding P-0040, N1-0290, I0-0053 and ERC AdG HIMMS.

## References

1. Zurek, W. Cosmological experiments in superfluid helium? *Nature* **317**, 505 (1985).
2. Kibble, T. W. B. Topology of cosmic domains and strings. *Journal Of Physics A-Mathematical And General* **9**, 1387–1398 (1976).
3. Schreiber, M. *et al.* Observation of many-body localization of interacting fermions in a quasirandom optical lattice. *Science* **349**, 842–845 (2015).
4. Wei, K. X., Ramanathan, C. & Cappellaro, P. Exploring Localization in Nuclear Spin Chains. *arXiv* (2016) doi:10.48550/arxiv.1612.05249.
5. Yusupov, R. *et al.* Coherent dynamics of macroscopic electronic order through a symmetry breaking transition. *Nat Phys* **6**, 681–684 (2010).
6. Stojchevska, L. *et al.* Ultrafast Switching to a Stable Hidden Quantum State in an Electronic Crystal. *Science* **344**, 177–180 (2014).
7. Kranjec, A. *et al.* Electronic Dislocation Dynamics in Metastable Wigner Crystal States. *Symmetry* **14**, 926 (2022).

8. Gerasimenko, Y. A., Karpov, P., Vaskivskiy, I., Brazovskii, S. & Mihailovic, D. Intertwined chiral charge orders and topological stabilization of the light-induced state of a prototypical transition metal dichalcogenide. *Npj Quantum Mater* **4**, 1–9 (2019).
9. Cho, D. *et al.* Nanoscale manipulation of the Mott insulating state coupled to charge order in 1T-TaS<sub>2</sub>. *Nat Commun* **7**, 10453 (2016).
10. Ma, L. *et al.* A metallic mosaic phase and the origin of Mott-insulating state in 1T-TaS<sub>2</sub>. *Nat Commun* **7**, 1–8 (2016).
11. Brazovskii, S., Brun, C., Wang, Z.-Z. & Monceau, P. Scanning-tunneling microscope imaging of single-electron solitons in a material with incommensurate charge-density waves. *Phys Rev Lett* **108**, 096801 (2012).
12. Mraz, A. *et al.* Manipulation of fractionalized charge in the metastable topologically entangled state of a doped Wigner crystal. *Nat. Commun.* **14**, 8214 (2023).
13. Salgado, R. *et al.* Low-frequency noise spectroscopy of charge-density-wave phase transitions in vertical quasi-2D 1T-TaS<sub>2</sub> devices. *Appl Phys Express* **12**, 037001 (2019).
14. Geremew, A. K., Rumyantsev, S., Debnath, B., Lake, R. K. & Balandin, A. A. High-frequency current oscillations in charge-density-wave 1T-TaS<sub>2</sub> devices: Revisiting the “narrow band noise” concept. *Appl Phys Lett* **116**, 163101 (2020).
15. Wilson, J. A., Salvo, F. J. D. & Mahajan, S. Charge-density waves and superlattices in the metallic layered transition metal dichalcogenides. *Adv Phys* **24**, 117–201 (1975).
16. Sipos, B., Berger, H., Forro, L., Tutis, E. & Kusmartseva, A. F. From Mott state to superconductivity in 1T-TaS<sub>2</sub>. *Nat Mater* **7**, 960–965 (2008).
17. Bozin, E. S. *et al.* Crystallization of polarons through charge and spin ordering transitions in 1T-TaS<sub>2</sub>. *Nat. Commun.* **14**, 7055 (2023).
18. Rossnagel, K. Suppression and emergence of charge-density waves at the surfaces of layered 1 T-TiSe<sub>2</sub> and 1 T-TaS<sub>2</sub> by in situ Rb deposition. *New J Phys* **12**, 125018–38 (2010).
19. Vodeb, J. *et al.* Configurational electronic states in layered transition metal dichalcogenides. *New J Phys* **21**, 083001 (2019).
20. Zong, A. *et al.* Ultrafast manipulation of mirror domain walls in a charge density wave. *Sci Adv* **4**, eaau5501 (2018).
21. Ravník, J. *et al.* Chiral domain dynamics and transient interferences of mirrored superlattices in nonequilibrium electronic crystals. *Sci. Rep.* **13**, 19622 (2023).
22. Park, J. W., Lee, J. & Yeom, H. W. Zoology of domain walls in quasi-2D correlated charge density wave of 1T-TaS<sub>2</sub>. *Npj Quantum Mater* **6**, 32 (2021).
23. Park, J. W., Cho, G. Y., Lee, J. & Yeom, H. W. Emergent honeycomb network of topological excitations in correlated charge density wave. *Nat Commun* **10**, 1–7 (2019).

24. Pretko, M. & Radzihovsky, L. Fracton-Elasticity Duality. *Phys Rev Lett* **120**, 195301 (2018).
25. Pretko, M. Emergent gravity of fractons: Mach's principle revisited. *Phys Rev D* **96**, 024051–16 (2017).
26. Liu, G., Rumyantsev, S., Bloodgood, M. A., Salguero, T. T. & Balandin, A. A. Low-Frequency Current Fluctuations and Sliding of the Charge Density Waves in Two-Dimensional Materials. *Nano Lett* **18**, 3630–3636 (2018).
27. Weissman, M. B. 1/f noise and other slow, nonexponential kinetics in condensed matter. *Rev. Mod. Phys.* **60**, 537–571 (1988).
28. Grassler, T. *Noise in Nanoscale Semiconductor Devices*. (Springer, 2020). doi:10.1007/978-3-030-37500-3.
29. Vaskivskyi, I. *et al.* Controlling the metal-to-insulator relaxation of the metastable hidden quantum state in 1T-TaS<sub>2</sub>. *Sci. Adv.* **1**, e1500168 (2015).
30. Vodeb, J. *et al.* Non-equilibrium quantum domain reconfiguration dynamics in a two-dimensional electronic crystal and a quantum annealer. *Nat. Commun.* **15**, 4836 (2024).
31. Ravník, J., Vaskivskyi, I., Mertelj, T. & Mihailović, D. Real-time observation of the coherent transition to a metastable emergent state in 1T-TaS<sub>2</sub>. *Phys Rev B* **97**, e1400173 (2018).
32. Prem, A., Pretko, M. & Nandkishore, R. M. Emergent phases of fractonic matter. *Phys Rev B* **97**, 085116 (2018).
33. Anderson, P. W. Through the Glass Lightly. *Science* **267**, 1615–1616 (1995).
34. Gerasimenko, Y. A. *et al.* Quantum jamming transition to a correlated electron glass in 1T-TaS<sub>2</sub>. *Nat Mater* **317**, 505–1083 (2019).
35. Schlör, S. *et al.* Correlating Decoherence in Transmon Qubits: Low Frequency Noise by Single Fluctuators. *Phys. Rev. Lett.* **123**, 190502 (2019).